Research Article
Volume 9:5, 2023

Journal of Antimicrobial Agents

ISSN: 2472-1212 Open Access

The Antibacterial Activity of Co–Er Ferrite/Graphene Nanocomposites and their Structural and Magnetic Properties

Amira S Shafaay*, Ebtesam E Ateia, MK Abdelamksoud and MM Arman

Department of Physics, Cairo University, Giza, Egypt

Abstract

$CoEr_{0.0.25}Fe_{1.975}O_4$, $CoFe_2O_4$/0.1GR, and $CoEr_{0.0.25}Fe_{1.975}O_4$/0.1GR nanoparticles were synthesized by using citrate auto combustion technique. The structure, morphology, magnetic and thermo-electrical properties of obtained nanocomposites have been examined using the X-ray diffraction technique, Fourier-Transform Infrared Spectroscopy (FT-IR), high-resolution transmission electron microscopy and vibrating sample magnetometer. Introducing graphene into the $CoFe_2O_4$ decreases the particle size and increases the magnetization of the system. The increase in the magnetic moment and hence the saturation magnetization can be attributed to the grafting of functional groups or adatoms to the graphene planes or to the edge bonds. The main mechanism of adatom chemisorption on graphene is breaking the π bonds and producing an additional σ bond. While dual doping with rare earth Er^{3+}/graphene decreases the saturation magnetization of the composites from 70.336 to 36.285 emu/g. However, the decrease in all magnetic parameters for $CoEr_{0.025}Fe_{1.975}O_4$/0.1GR can be attributed to the doping of rare earth ions (Er^{3+}) that decreases the parallelism between the magnetic moments at the B site. This decrease offsets to some extent the increase of unpaired spins resulting due to the addition of graphene.

The application of the thermoelectric concept will help to deal with two main global issues, the increasing demand for energy with all the developments and the drastic climate changes. Consequently, the Seebeck coefficient as a function of temperature is scrutinizing. Graphene is one of the main issues for increasing the efficiency of antibacterial activity. It is obvious that the $CoFe_2O_4$/0.1GR sample has a strong antibacterial activity against *Pseudomonas aervginosa.*

Keywords: Graphene • Rare earth • Seebeck coefficient • Antibacterial • Electrical properties

Introduction

Magnetic properties of spinel ferrite nanoparticles have been intensively investigated due to their extraordinary properties. In the family of spinel ferrites, $CoFe_2O_4$ nano ferrite possesses numerous applications in the fields of magneto-recording media, catalysis, medicine, gas sensors and high-frequency devices [1-5]. Cobalt ferrites possessing a partially inverse spinel structure and have affirmative anisotropy constant, remarkable mechanical hardness, high resistivity, and good chemical stability [6-9].

The ideal graphene is classified as diamagnetic material. On the other hand, the para magnetism is occurred in real graphene due to the existence of edges and/or other defects.

Meanwhile, according to the theoretical and experimental investigations the magnetic moment of graphene increases due to the presence of defects [10-12]. This increase is related to the increase of unpaired spins. However, theoretically expected magnetic coupling is not always detected in practice and its existence is very disputable [13]. Theoretical estimation of ferro and anti-ferromagnetism usually elucidate these various possibilities of magnetic coupling by the bipartite lattice of graphene. If magnetism is generating from defects in one sub lattice of graphene, the ferromagnetism is possible. While, the anti-ferromagnetic is occurred when the defects are distributed in different sub lattices. Consequently, in practice, the antiferromagnetic state is most predominant.

The alternative source of magnetism is originating from the localized edge states of graphene. The carbon structures that consist of zigzag edges can be magnetic as confirmed from the first

***Address for Correspondence:** Amira S Shafaay, Department of Physics, Cairo University, Giza, Egypt, Tel: 201224615902; E-mail: amirasamy10184@gmail.com*

Received: 10 June, 2023, Manuscript No. ANTIMICRO-23-102026**; Editor assigned:** 13 June, 2023, PreQC No. ANTIMICRO-23-102026 (PQ); **Reviewed:** 28 June, 2023, QC No. ANTIMICRO-23-102026; **Revised:** 10 October, 2023, Manuscript No. ANTIMICRO-23-102026 (R); **Published:** 18 October, 2023, DOI: 10.37421/2472-1212.2023.9.319

principles and mean-field theory calculations [14]. The theoretical calculations show that in zigzag ribbons localized electron spins is polarized, leading to ferromagnetism [15]. In general, almost all possible defects can lead to the magnetic moment due to perturbation in the graphene structure. However, the complete mechanism leading to magnetic properties is still a matter of discussion.

The fascinating physical properties of Rare-Earth (RE) doped ferrites have attracted many researchers. The rare-earth lanthanides are good electrical insulators with low conductivity. The effect of RE ions substitution such as La, Sm, Gd, Dy, Yb, and Ce for Fe^{3+} ion was scrutinized by many investigators [16-20]. Rare earth ions such as Er^{3+} have unpaired $4f^{12}$ electrons, and their magneto crystalline anisotropy is related to the 4f-3d coupling between the rare earth and transition metal ions. The properties of the nano ferrite particles can be improved by the substitution of the appropriate amount of RE ions in place of Fe ions in the octahedral sites [21].

In the present study, an attempt is made to study the effect of dual doping with Er^{3+}/grapheme on the structural, electrical and magnetic properties of the investigated samples.

Materials and Methods

The stoichiometric quantities of Fe $(NO_3)_3.9H_2O$ and Co $(NO_3)_2.4H_2O$ and Er $(NO_3)_3.6H_2O$ were prepared by using the citrate auto combustion technique as shown in Figure 1 [22]. The structure and crystallite sizes were tested by X-Rays Diffractometer (XRD) using Diano corporation of target Cu-Kα (λ=1.5424 Å). The morphology of the samples was studied by High Resolution Transmission Scanning Electron Microscopy (HRTEM) attached with EDAX unit (Energy Dispersive X-ray Analyses). The magnetization M (emu/g) was measured at room temperature using a Vibrating Sample Magnetometer (VSM) model Lake Shore 7410.

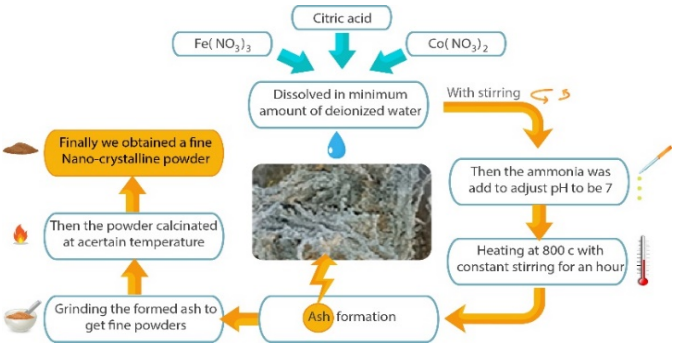

Figure 1. Flowchart of the preparation methods.

The Seebeck coefficient as a function of temperature is one of the crucial methods for scrutinizing the electronic properties of materials. The classification of charge carriers and the mechanisms of electric conduction were obtained from thermoelectric power measurements. It can be calculated using the following relation [23].

$$S = \lim_{\Delta T \to 0} \frac{\Delta V}{\Delta T} = \frac{dV}{dT} \quad \text{------ (1)}$$

Where ΔV was the potential difference produced due to the temperature difference ΔT between the two points.

Results and Discussion

XRD technique has been used to ratify the formation of phase in the prepared samples with general formula $CoFe_2O_4$, $CoEr_{0.0.25}Fe_{1.975}O_4$, $CoFe_2O_4$/0.1GR, and $CoEr_{0.0.25}Fe_{1.975}O_4$/0.1GR nanoparticles. The XRD chart is depicted in Figure 2. The diffraction peaks recognized at the diffraction angles nearer to 30.19°, 35.55°, 37.15°, 43.24°, 53.34°, 57.14°, 62.69°, 71.3° and 74.18° in all XRD patterns are indexed with the miller indices (220), (311), (222), (400), (422), (511), (440), (620) and (533). These are consistent with the JCPDS card no. 00-002-1045, belonging to the Fd3m space group.

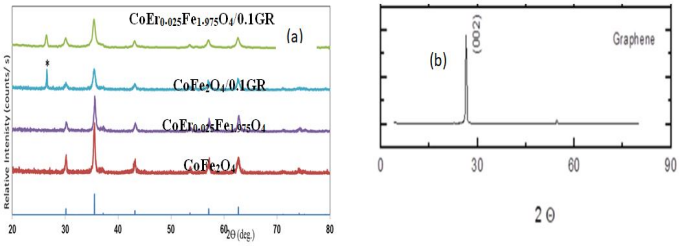

Figure 2. (a) XRD patterns of the samples: $CoFe_2O_4$, $CoEr_{0.025}Fe_{1.975}O_4$, $CoEr_{0.025}Fe_{1.975}O_4$/0.1GR and $CoFe_2O_4$/0.1GR, (b) Graphene.

The sharp peak (*) at approximately 26.0°, (002) reflection, is compared to the graphene X-ray spectrum as shown in Figure 2.

This noticing ratifies the existence of Graphene (GR) nanoparticles in the cobalt spinel ferrite network. The indexed diffraction planes are proportionate with JCPDS card no. (04-015-9499). The broadening of the peaks indicates the increase in the surface-to-volume ratio of the prepared samples.

The average crystallite size (D_{avg}) is calculated from the Scherrer equation as mentioned by E. Ateia, et al.

It is clearly seen that the peak intensity and width of the peaks increase with adding Er^{3+} content and graphene in cobalt ferrite nanoparticles.

The decrease of crystallite size with the addition of rare-earth ions (Er^{3+}) is due to the larger bond energy of RE^{3+}–O^{2-} compare to that of Fe^{3+}–O^{2-}. In other words, more energy is needed to force RE^{3+} ions with larger radii (0.89 Å) into the octahedral lattices and form the bond oxygen anion. Consequently, it is expected that rare-earth ions doped ferrite nanoparticles show lower particle size as well as higher thermal stability compared to the parent sample. Additionally, more energy is needed for the Co/Er samples to complete grain crystallization and growth. This trend was discussed by a number of authors.

The HRTEM images of the $CoEr_{0.025}Fe_{1.975}O_4$, $CoFe_2O_4$/0.1GR, and $CoEr_{0.025}Fe_{1.975}O_4$/0.1GR nano-composites are shown in Figure 3. As shown from the figure that the particles are agglomerated, spherical and nano-sized. Moreover, the doping of Er^{3+} ions decreases

the size of the grains. Illustrates that the flake-like graphene nano-sheets are decorated with $CoEr_{0.025}Fe_{1.975}O_4$ nanoparticles with some formation of aggregations. The Selected-Area Electron Diffraction (SAED) pattern is illustrated in Figure 3. The characteristic of nano poly crystalline structure of the synthesized samples is ratified from the bright Spots Arrangement That Detected in (SAED) pattern. The average particle sizes are detected from the histograms and the obtain data agrees well with XRD data.

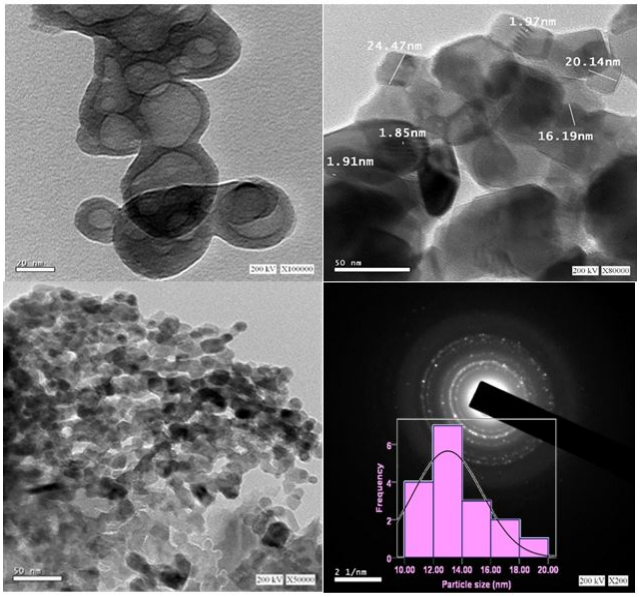

Figure 3. HRTEM of the samples $CoEr_{0.0.25}Fe_{1.975}O_4$, $CoFe_2O_4$/0.1GR, and $CoEr_{0.0.25}Fe_{1.975}O_4$/0.1GR SAED with inset represents average particles distribution and d spacing.

Figure 4 shows the mapping of $CoFe_{1.075}Er_{0.025}O_4$ with color scheme. As reveal, there is a homogenous distribution of Cobalt (Co), Iron (Fe), Erbium (Er) and Oxygen (O) throughout the materials. Furthermore, the cobalt and iron content levels of this sample are measured by Inductively Coupled Plasma analysis (ICP). The atomic ratio of Co/Fe is found to be 0.47.

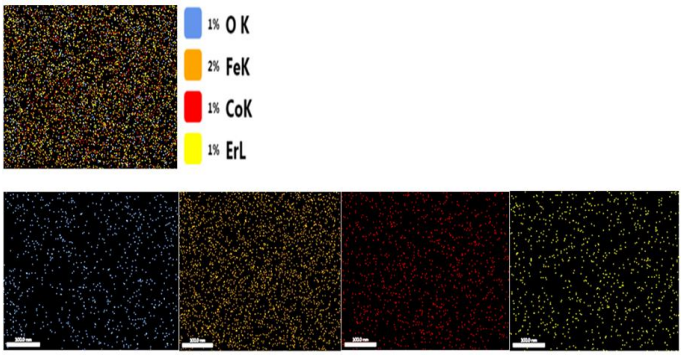

Figure 4. Mapping of $CoFe_{1.075}Er_{0.025}O_4$ with color scheme.

Figure 5 The Energy-Dispersive X-Ray Spectroscopy (EDAX) deliberately investigates the detailed chemical composition of the studied samples. The characteristic peaks in the spectrum comprise Co, Fe, Er, C and O. The atomic percentage (at %) and weight percentage (wt %) of constituent elements, are presented in the inset of the figures. The carbon and oxygen are presented in the sample as detected from Figure 5, which emphasize the existence of graphene in the studied system.

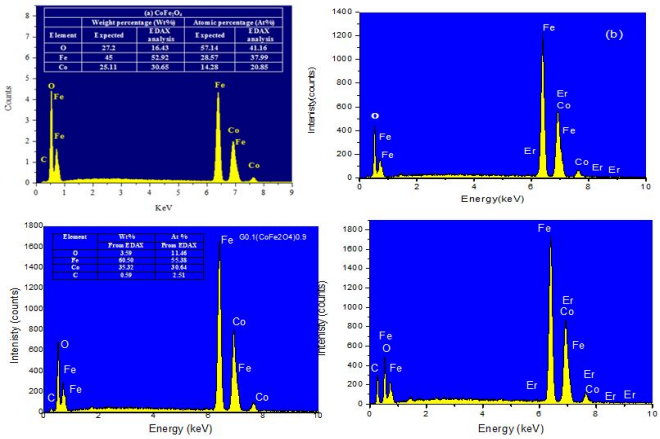

Figure 5. The Energy-Dispersive X-ray spectroscopy (EDAX) for (a) $CoFe_2O_4$, (b) $CoEr_{0.025}Fe_{1.975}O_4$, (c) $CoFe_2O_4$/0.1GR and (d) $CoEr_{0.025}Fe_{1.975}O_4$/0.1GR.

Fourier-Transform Infrared Spectroscopy (FT-IR) is studied to investigate the surface chemical compositions of the prepared samples. The corresponding data is illustrated in Figure 6. The FT-IR bands of the samples are detected in the range 600-500 cm^{-1} corresponds to the intrinsic stretching vibrations of the metal at the tetrahedral site. The stretching vibration at octahedral sites cannot be specified due to technical problems.

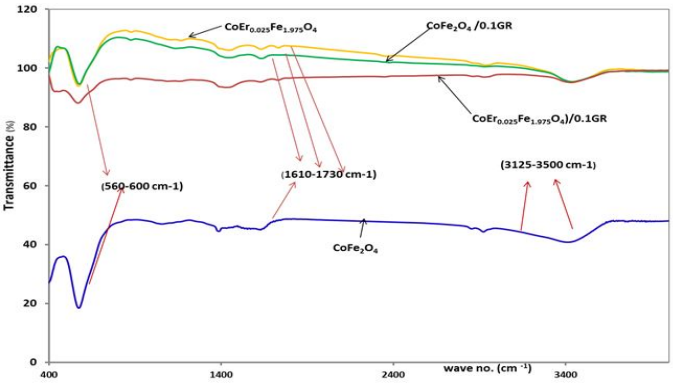

Figure 6. FTIR of $CoFe_2O_4$, $CoEr_{0.025}Fe_{1.975}O_4$, $CoEr_{0.025}Fe_{1.975}O_4$/0.1GR and $CoFe_2O_4$/0.1GR.

The peaks at 2917 cm^{-1} and 2937 cm^{-1} are attributed to C-H stretching vibration present in the sample. The broad stretching at 3125 cm^{-1} and 3500 cm^{-1} designates the mode of binding through OH group existing in the samples.

The peaks at 1727, 1569, 1405, 1232, and 1050 cm^{-1} can be assigned to the C=O, aromatic C=C, carboxy C-O, epoxy C-O, and C-O groups on the surface of graphene sheets, respectively.

For the graphene spectrum, the peaks at 3400 cm^{-1}, 1723 cm^{-1}, 1630 cm^{-1}, 1370 cm^{-1}, and 1060 cm^{-1} are attributed to the OH stretching vibrations of adsorbed water, C=O stretching vibrations of carboxyl or carbonyl groups, OH deformation vibrations of COOH

COOH groups, OH deformation vibrations of tertiary C-OH, and C-O stretching vibrations of epoxy groups, respectively.

Figure 7 shows the hysteresis loops of the investigated samples using a Vibrating Sample Magnetometer (VSM) at 300. It is clear that the magnetization for all investigated samples increases with the applied magnetic field until reaching saturation trend.

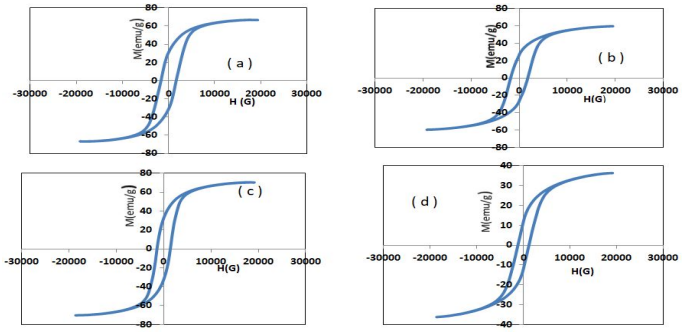

Figure 7. The hysteresis loops for (a) $CoFe_2O_4$, (b) $CoEr_{0.025}Fe_{1.975}O_4$, (c) $CoFe_2O_4$/0.1GR and (d) $CoEr_{0.025}Fe_{1.975}O_4$/0.1GR using a Vibrating Sample Magnetometer (VSM) at 300 K.

The rare-earth ions prefer to occupy the octahedral B site and are established by the suggested cation distribution as depicted in Table 1. According to the cation distribution, it is clear that Er^{3+} ions with a magnetic moment of 9 BM. occupy the octahedral site by replacing Fe^{3+} ions with a magnetic moment of 5 BM. The magnetization of the doped sample decreases compared to that of pure cobalt even the dopant cations have the magnetic moments larger than that of Fe^{3+} ions, as shown in Table 2 and Figure 7. This decrease is correlated with the weakening of the exchange interaction as well as B-B interaction. Additionally, the inclusion of Er^{3+} increases the Yafet-Kittel angle leads to a decrease in the saturation magnetism of the doped samples. The same behavior is reported for Tb^{3+} ions (μB=9.5 BM) when doped to $CoFe_2O_4$.

Samples	Crystallite size XRD (nm)	Particle size HRTEM (nm)	Cation distribution
$CoFe_2O_4$	31.37	-	$(Fe^{3+})\ (Co_2{}^{+}Fe^{3+})$
$CoFe_2O_4$/0.1GR	14.24	21	
$CoEr_{0.025}Fe_{1.975}O_4$	11.975	20	$(Co_2{}^{+}{}_{1-x}Fe^{3+}{}_x)\ (Co_2{}^{+}{}_x\ Er_yFe^{3+}{}_{2-x-y})$
$CoFe_{1.975}Er_{0.025}O_4/GR_{0.1}$	11.981	13	

Table 1. The values of the crystallite size, particle size and cation distribution for the investigated samples.

In general, almost all possible defects change the magnetic moment due to disruption in the graphene structure. This change is related to the increase of unpaired spins. If magnetism is generating from defects in one sub-lattice, the parallel magnetic ordering (ferromagnetism) is probable.

The increase in the magnetic moment and hence the saturation Magnetization (M_S) for $CoFe_2O_4$/0.1GR (high content of graphene) can be attributed to the grafting of functional groups or adatoms to the graphene planes or to the edge bonds. The main mechanism of adatom chemisorption on graphene is breaking the π bonds and producing an additional σ bond, thus, changing sp^2 to sp^3 hybridization. Obviously, such a process gradually leads to the appearance of the magnetic moment of graphene while it decreases its conductivity.

However, the decrease of magnetic parameters for $CoEr_{0.025}Fe_{1.975}O_4$/0.1GR can be attributed to that the doping of rare earth ions (Er^{3+}) decreases the parallelism at the B site. This decrease offsets to some extent the increase of unpaired spins resulting due to the addition of graphene.

The magnetic parameters as the coercivity (H_C), saturation Magnetization (M_S), remnant Magnetization (M_r), squareness (M_r/M_S) and magnetic moment (n_B) are determined and presented in Table 2. Generally, the net magnetic moment of the studied samples is determined by the distribution of the Co^{2+} and Fe^{3+}, Er^{3+} cations and graphene over octahedral and tetrahedral sites.

The sub-lattice experimental magnetic moment is calculated by using the following equation 2.

$$n_B = M_w \times M_S/5585 \quad (2)$$

Where M_w is the molecular weight of a particular ferrite composition. The experimental magnetic moment is tabulated in Table 2.

Composite	M_r (emu/g)	M_s (emu/g)	H_c (G)	M_r/M_s	Energy loss (erg/g)	Crystallite (nm)	n_B exp.
$CoFe_2O_4$	31.114	66.847	1641	0.465	337000	31.37	2.808
$CoFe_2O_4$/0.1GR	32.465	70.336	1411	0.462	278020	18.5	_
$CoEr_{0.025}Fe_{1.975}O_4$	26.626	59.618	1778	0.447	294420	11.975	2.534

$CoEr_{0.025}Fe_{1.975}O_4$/0.1GR	11.927	36.285	1187	0.329	124270	11.981	_

Table 2. The saturation Magnetization (M_s), the remnant Magnetization (M_r), the coercive field (H_C), squareness ratio (M_r/M_s), energy loss, crystallite size and experimental magnetic moment for the investigated samples.

As shown from the Table the magnetic parameters of the nanoparticles depend upon the crystallite size, magnetic moment and the number of unpaired electrons. As the size decreases, the surface area increases, as well as the surface energy and surface tension. This causes the exchange in the cationic preference and then increases the anti-site defects, consequently, the saturation magnetization decreases.

Generally, the spin-orbital coupling is much stronger in rare earth ions than the transition metal ions. Certainly, the highest coercively for $CoEr_{0.025}Fe_{1.975}O_4$, is due to the smallest particle size as well as the strong spin-orbital coupling of E^{r3}+ ion.

The application of the thermoelectric concept will help to deal with two significant global issues, the increasing demand for energy with all the developments and the extreme climate changes.

The temperature dependence of the Seebeck coefficient in the temperature range of 300 K to 750 K is presented in Figure 8. As shown from the figure, for all samples the Seebeck coefficient (α) is fluctuated between positive and negative values. This fluctuation of α indicates that majority charge carriers are of n-type, and p-type suggesting the conduction mechanism to be predominantly by electron and holes hopping respectively. Such type of behavior is also reported in the previous work. Moreover, the Seebeck coefficient decreases for Er^{3+} doped samples. The reduction in the population of the Fe^{3+} ions at the B-site is the main reason for the observed decrease of the Seebeck coefficient. The same trend has been reported for other rare earth substitution in Mg-Cd ferrite and Cu-Cd ferrite.

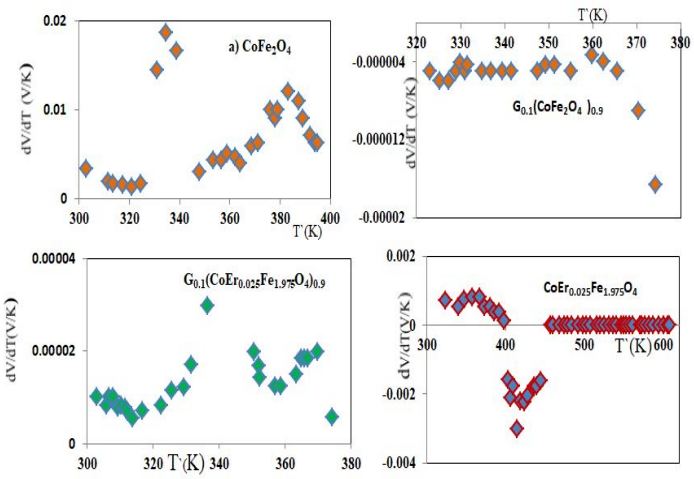

Figure 8. The temperature dependence of the Seebeck coefficient for the investigated samples.

The antibacterial activity of $CoFe_2O_4$/0.1GR and $CoEr_{0.025}Fe_{1.975}O_4$/0.1GR nanoparticles is investigated using a modified Kirby-Bauer disc diffusion method. The antibacterial activity was carried out against two kinds of bacteria: *Neisseria gonorrhoeae* and Pseudomonas aervginosa as shown in Figure 9.

It is obvious that the $CoFe_2O_4$/0.1GR sample does not possess antibacterial activity against *Neisseria gonorrhoeae* while it has a strong antibacterial activity against *Pseudomonas aervginosa*. Figure 9 shows the variation in the inhibition zone caused by the synthesized samples. Graphene is one of the main issues for increasing the efficiency of antibacterial activity. The antibacterial activity studies reveal that the efficiency is maximum (62%). This can be attributed to the high content of graphene enables more vacancy to interact with bacteria, leading to a better antibacterial efficiency.

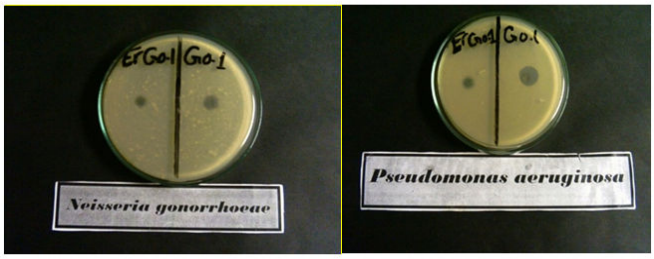

Figure 9. Antibacterial activity against *Neisseria gonorrhea* and *Pseudomonas aervginosa* for the $CoFe_2O_4$/0.1GR and $CoEr_{0.025}Fe_{1.975}O_4$/0.1GR.

Conclusion

By using the citrate auto combustion method, graphene substituted $CoFe_2O_4$ and graphene substituted rare earth $CoFe_2O_4$ were successfully prepared with a small crystal size (12 nm). $CoFe_2O_4$/0.1GR (high concentration) shows ferromagnetic behavior. The addition of a high content of graphene increases the magnetization of the system due to the presence of edges and other defects. Graphene based $CoFe_2O_4$ magnetic samples demonstrate an improvement in the structural properties. The conjunction of graphene into the cobalt nanocomposites enhances the cation redistribution, changes the morphology, and decreases the crystallite sizes of the investigated samples.

The doping of rare earth ions (Er^{3+}) decreases the parallelism between the magnetic moments at the B site. This decrease offsets to some extent the increase of unpaired spins resulting due to the addition of graphene.

The fluctuation of the Seebeck coefficient sign between (+)ve and (–)ve in cobalt rare earth ferrite means that the two conduction mechanisms take place simultaneously. $CoFe_2O_4$/0.1GR shows an inhibition zone of diameter=16 mm (With efficiency=62%) against *Pseudomonas aervginosa*. Thus, one can be recommended it for biomedical applications.

References

1. Yi, Dong Kee, Su Seong Lee, and Jackie Y Ying. "Synthesis and applications of magnetic nanocomposite catalysts." *Chem Mater* 18 (2006): 2459-2461.
2. Kale, Swati B, Sandeep B Somvanshi, MN Sarnaik, and SD More, et al. "Enhancement in surface area and magnetization of $CoFe_2O_4$ nanoparticles for targeted drug delivery application." *AIP Conf Proc* 1953 (2018).
3. Reddy, CV Gopal, SV Manorama, and VJ Rao. "Semiconducting gas sensor for chlorine based on inverse spinel nickel ferrite." *Sens Actuators B Chem* 55 (1999): 90-95.
4. Kharat, Prashant B, Sandeep B Somvanshi, Jitendra S Kounsalye, and Suraj S Deshmukh, et al. "Temperature dependent viscosity of cobalt ferrite/ethylene glycol ferrofluids." *AIP Conf Proc* 1942 (2018).
5. Rondinone, Adam J, Chao Liu, and Z John Zhang. "Determination of magnetic anisotropy distribution and anisotropy constant of manganese spinel ferrite nanoparticles." *J Phys Chem B* 105 (2001): 7967-7971.
6. Slonczewski, JC. "Anisotropy and magnetostriction in magnetic oxides." *J Appl Phys* 32 (1961): S253-S263.
7. Gul IH, and A Maqsood. "Structural, magnetic and electrical properties of cobalt ferrites prepared by the sol–gel route." *J Alloys Compd* 465 (2008): 227-231.
8. Liu, Chao, Bingsuo Zou, Adam J Rondinone, and Z John Zhang, et al. "Chemical control of superparamagnetic properties of magnesium and cobalt spinel ferrite nanoparticles through atomic level magnetic couplings." *J Am Chem Soc* 122 (2000): 6263-6267.
9. Matte, HSS Ramakrishna, KS Subrahmanyam, and CNR Rao. "Novel magnetic properties of graphene: Presence of both ferromagnetic and antiferromagnetic features and other aspects." *J Phys Chem C* 113 (2009): 9982-9985.
10. Nair, RR, M Sepioni, I-Ling Tsai, and O Lehtinen, et al. "Spin-half paramagnetism in graphene induced by point defects." *Nat Phys* 8 (2012): 199-202.
11. Ugeda, Miguel M, Ivan Brihuega, Francisco Guinea, and Jose M Gomez-Rodriguez, et al. "Missing atom as a source of carbon magnetism." *Phys Rev Lett* 104 (2010): 096804.
12. Yazyev, Oleg V, and Lothar Helm. "Defect-induced magnetism in graphene." *Phys Rev B* 75 (2007): 125408.
13. Kuzemsky, A. L. "Unconventional and exotic magnetism in carbon-based structures and related materials." *Int J Mod Phys B* 27 (2013): 1330007.
14. Bar, Marcus, BA Schubert, Bjorn Marsen, and Regan G Wilks, et al. "Cliff-like conduction band offset and KCN-induced recombination barrier enhancement at the CdS/ Cu_2ZnSnS_4 thin-film solar cell heterojunction." *Appl Phys Lett* 99 (2011).
15. Nikumbh AK, RA Pawar, DV Nighot, and GS Gugale, et al. "Structural, electrical, magnetic and dielectric properties of rare-earth substituted cobalt ferrites nanoparticles synthesized by the co-precipitation method." *J Magn Magn Mater* 355 (2014): 201-209.
16. Yehia, M, SM Ismail, and A Hashhash. "Structural and magnetic studies of rare-earth substituted nickel ferrites." *J Supercond Nov Magn* 27 (2014): 771-774.
17. Rahimi-Nasrabadi, Mehdi, Mohsen Behpour, Ali Sobhani-Nasab, and Mansoureh Rangraz Jeddy, et al. "Nanocrystalline Ce-doped copper ferrite: Synthesis, characterization, and its photocatalyst application." *J Mater Sci Mater Electron* 27 (2016): 11691-11697.
18. Zhou, Jun, Junfeng Ma, Chong Sun, and Lijin Xie, et al. "Low-Temperature Synthesis of $NiFe_2O_4$ by a Hydrothermal Method." *J Am Ceram Soc* 88 (2005): 3535-3537.
19. Rezlescu, N, E Rezlescu, C Pasnicu, and ML Craus, et al. "Effects of the rare-earth ions on some properties of a nickel-zinc ferrite." *J Phys Condens Matter* 6 (1994): 5707.
20. Ateia, Ebtesam E, MK Abdelmaksoud, MM Arman, and Amira S Shafaay, et al. "Comparative study on the physical properties of rare-earth-substituted nano-sized $CoFe_2O_4$." *Appl Phys* A 126 (2020): 1-10.
21. Yoon, Yo-Seop, Won-Yong Lee, No-Won Park, and Gil-Sung Kim, et al. "Cross-plane thermoelectric Seebeck coefficients in nanoscale Al_2O_3/ZnO superlattice films." *J Mater Chem* C 7 (2019): 1670-1680.

How to cite this article: Shafaay, Amira S, Ebtesam E Ateia, MK Abdelamksoud and MM Arman. "The Antibacterial Activity of Co–Er Ferrite/ Graphene Nanocomposites and their Structural and Magnetic Properties." *J Antimicrob Agents* 9 (2023): 319